

# Numerical and experimental study of flow structure and heat release distribution in a stratified swirl flame with high-speed PIV and OH\* measurements

Cite as: AIP Advances 11, 075311 (2021); <https://doi.org/10.1063/5.0056312>

Submitted: 08 May 2021 • Accepted: 15 June 2021 • Published Online: 07 July 2021

Sheng Meng, Shizhi Wu and  Man Zhang



View Online



Export Citation



CrossMark

## ARTICLES YOU MAY BE INTERESTED IN

[OH\\* and CH\\* chemiluminescence characteristics in low swirl methane-air flames](#)

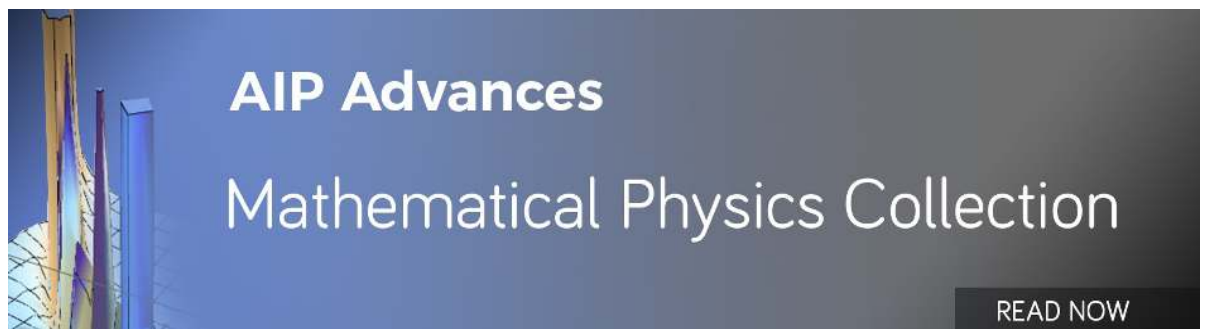
AIP Advances 10, 055318 (2020); <https://doi.org/10.1063/5.0002660>

[Multi-bifurcation behaviors of stability regimes in a centrally staged swirl burner](#)

Physics of Fluids 33, 095121 (2021); <https://doi.org/10.1063/5.0063562>

[A combined oscillation cycle involving self-excited thermo-acoustic and hydrodynamic instability mechanisms](#)

Physics of Fluids 33, 085122 (2021); <https://doi.org/10.1063/5.0057521>



AIP Advances  
Mathematical Physics Collection

READ NOW

# Numerical and experimental study of flow structure and heat release distribution in a stratified swirl flame with high-speed PIV and OH\* measurements

Cite as: AIP Advances 11, 075311 (2021); doi: 10.1063/5.0056312

Submitted: 8 May 2021 • Accepted: 15 June 2021 •

Published Online: 7 July 2021



View Online



Export Citation



CrossMark

Sheng Meng, Shizhi Wu, and Man Zhang<sup>a)</sup> 

## AFFILIATIONS

AECC Commercial Aircraft Engine CO., Ltd., 200241 Shanghai, China

<sup>a)</sup> Author to whom correspondence should be addressed: [flamegroup2020@163.com](mailto:flamegroup2020@163.com)

## ABSTRACT

Stratified swirled flame is widely used in gas turbines and aero engines to achieve low emissions. However, the limitation of implementing laser diagnostic in real combustors acquires more accurate measurements of field information in the flame, especially the unsteady heat release, which relates to a lot of important phenomena, such as combustion instability and blow-off. The present study employs large eddy simulation (LES) combined with a detailed OH\* chemiluminescence reaction mechanism to validate the chemiluminescent image of OH\* in a stratified swirled flame at the atmosphere condition. 10 kHz particle image velocimetry images and OH\* filtered images are recorded during the experiment. The heat release and flow structure of the stratified swirled flame at two different fuel stratification ratios show distinguished flame shapes. In general, the velocity results of LES have good agreement with the measurement. The numerical OH\* and heat release comparison reveals a strong dependence on the local strain rate and turbulence level of OH\* emissions. It is also noticed that the wrong flame shapes may be deduced from the Abel inversed OH\* image since the signals are weak in the outer recirculation zone. This indicates that the strain rate in different regions of stratified swirl flame has a significant impact on OH\* signal distribution. The results provide insight into the ability of chemiluminescent emissions, such as OH\*, to indicate heat release in more complex industrial flames.

© 2021 Author(s). All article content, except where otherwise noted, is licensed under a Creative Commons Attribution (CC BY) license (<http://creativecommons.org/licenses/by/4.0/>). <https://doi.org/10.1063/5.0056312>

## I. INTRODUCTION

Stratified swirled flames are commonly used in lean pre-mixed prevaporized (LPP) combustors for gas turbines or aero engines.<sup>1</sup> The concentrically staged fuel/oxidizer fields achieve flexible operation conditions and low emissions. Non-premixed pilot flame is typically located in the center of the combustor for flame stabilization. Together with radical main premixed flame, it makes a globally lean partially premixed flame. Swirling flows also assist flame stabilization by inducing shear layers and recirculation zones.<sup>2,3</sup> This type of flame often has strong spatial gradients in the equivalence ratio or mixture fraction, which influence the flame structure and unsteady combustion. To maximize the usage of

numerical simulations in the combustor design phase for cost reduction, understanding and modeling the dynamics of turbulent stratified swirled flames are important.

Heat release is an important indicator in combustion dynamics. It is correlated with many unsteady phenomena, such as combustion instability and flame flashback.<sup>4–8</sup> In both cases, the heat release rate of the flame has to be measured. However, the direct measurement of the heat release rate is not accessible. In many cases, it is indirectly measured through the chemiluminescent species CH\* and OH\*.<sup>9–12</sup> Chemiluminescence is the light emitted from electronically excited atoms or molecules.

Laser-induced fluorescence signals are also widely used to locate the heat release zone.<sup>13–15</sup> However, due to the limitation of

the observation window and quenching issue in high pressure or high-temperature conditions,<sup>16</sup> the usage of those diagnostic technologies is still challenging in a practical combustor. Otherwise, the self-excited states of radicals provide an alternative choice in those complex and extreme conditions. For the combustion of hydrocarbons, excited-state radicals are mainly  $\text{OH}^*$  with a radiation wavelength of 308 nm and  $\text{CH}^*$  with a radiation wavelength of 431 nm. Since chemiluminescence originates from the reaction zone of the flame, it is commonly assumed to characterize the heat release rate of flames.

The radiation from the excited hydroxyl radical  $\text{OH}^*$  is the most distinct radiation of many flames in the UV region. However, a quantitative comparison of the line-of-sight integrated flame radiation with numerical simulation is not easy.  $\text{OH}^*$  radiation is not a direct output of common numerical simulations. To overcome this, four methods for simulating  $\text{OH}^*$  radiation of a laminar hydrogen-oxygen jet flame were presented by Fiala.<sup>17</sup> The detailed chemistry radiation model (DC) includes  $\text{OH}^*$  as a separate species in the detailed chemical reaction mechanism, in which the non-equilibrium of  $\text{OH}^*$  can be evaluated. The disadvantages of DC are that additional equations for the species  $\text{OH}^*$  have to be solved during the simulation run and the computational cost is higher than other model approaches. Simplifying and including the absorption effect, Fiala developed the equilibrium filtered radiation model especially for the high-temperature flame, in which thermal excitation dominates. Lauer<sup>18,19</sup> stated that the integrated chemiluminescence might be an applicable indicator of the integrated heat release rate in turbulent premixed methane-air flames.

Recently, Bedard<sup>20</sup> employed detailed kinetics including the emitting species to simulate the combustion instability and then compared that to experimental spectral measurements in a practical high-pressure rocket combustor. Optically thin gas and medium were assumed in simulation to avoid reabsorption of  $\text{CH}^*$  and  $\text{OH}^*$ . The author concluded that  $\text{CH}^*$  chemiluminescence may provide a better representation of the combustion reaction due to its low ground state concentration. Nevertheless, the results also suggested that the location of heat release is not accurately represented by either of the species or a combination thereof. He<sup>21</sup> investigated the  $\text{OH}^*$  chemiluminescence and heat release in laminar methane-oxygen co-flow diffusion flames. The production pathway of  $\text{OH}^*$  chemiluminescence showed that the reaction  $\text{H} + \text{O} + \text{M} = \text{OH}^* + \text{M}$  (R1) is the major source of  $\text{OH}^*$  chemiluminescence. The  $\text{OH}^*$  distribution can be used to characterize the flame combustion condition. To improve the quantitative relationship between the chemiluminescence intensity and heat release rate, Liu<sup>22</sup> predicted heat release rate distribution according to  $\text{OH}^*$  and  $\text{CH}^*$  radical intensities based on deep learning.

The previous studies of quantitative comparison of simulated  $\text{OH}^*$  and measurement mainly focused on non-stratified flames.

This paper uses the detailed GRI 3.0 mechanism combined with the  $\text{OH}^*$  chemiluminescence reaction mechanism to simulate a stratified swirled methane/air flame at the atmosphere condition. To validate the reliability of simulated  $\text{OH}^*$ , experimental measurements using 10 kHz PIV and 10 kHz filtered  $\text{OH}^*$  images are conducted. Based on the numerical simulation and experimental results, it allowed us to gain a deeper understanding of the chemiluminescence mechanism in different fuel stratification ratios of flame.

## II. EXPERIMENTAL SETUP

The experimental apparatus employed in this paper was at the Southern University of Science and Technology [Fig. 1(a)]. A typical picture of the flame is presented in Fig. 1(b). The air inlet section shown in Fig. 1(a) consists of a tube with  $H_1 = 260$  mm and  $d = 100$  mm. A compressed air system was connected to the inlet section, generating a maximum airflow of 0.5 kg/s in the atmosphere. The height of the combustion section is 200 mm, and the width is 105 mm. It consists of two opposed observation windows with an area of  $100 \times 150$  mm<sup>2</sup> [see Fig. 1(c)]. 10 kHz Particle Image Velocimetry (PIV) was implemented by using a QuasiModo (Spectral Energies) diode-pumped Nd:YAG laser with a maximum power output of about 600 mJ per pulse at 532 nm. A combination of a series of cylindrical lenses was used to create the PIV laser sheet of 0.5 mm. The flow was seeded with  $\text{Al}_2\text{O}_3$  particles with a mean diameter of 1  $\mu\text{m}$  using a fluidized-bed particle seeder. A Phantom V2012 camera (1024  $\times$  800 pixels at 20 kHz) was used with

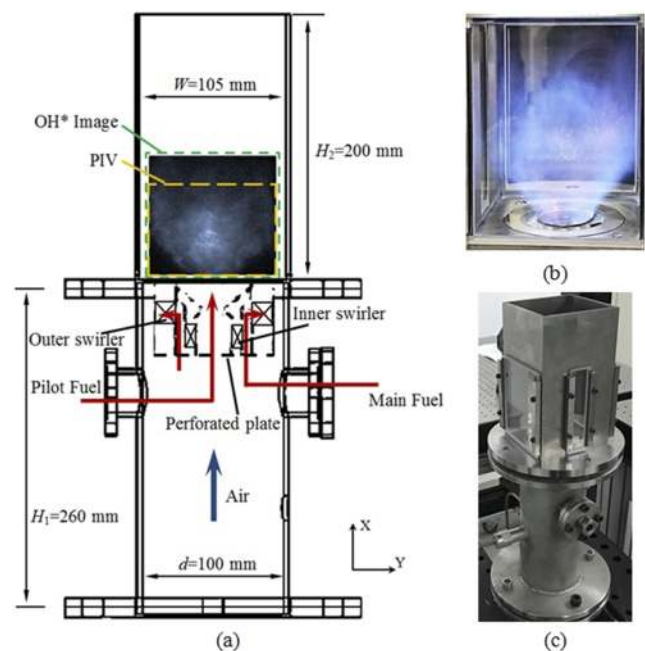


FIG. 1. (a) Schematic of the stratified swirled burner, (b) picture of the typical flame, and (c) picture of the inlet and combustion section.

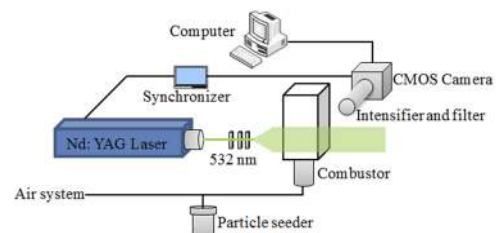


FIG. 2. Optical setup for PIV and  $\text{OH}^*$  measurements. In the PIV measurement, the intensifier and  $\text{OH}^*$  filter are removed.

**TABLE I.** Summary of operation conditions.

Case	Total airflow rate (g/s)	Total methane flow rate (g/s)	The pilot flame equivalent ratio	The main flame equivalent ratio	Fuel stratification ratio (FSR)
S1	160	1.191	18	0.7	1:1
S2	290	1.191	2	0.7	1:9

a 105 mm Micro-Nikkor lens to image the PIV frames at 10 kHz (with minimum straddling times approaching 10  $\mu$ s). The laser and camera were externally triggered using a delay generator (Model DG645). The same camera was used to record the OH\* images through an image intensifier (Lambert Instruments) with a band-pass filter of 310  $\pm$  10 nm. The OH\* images were also captured at 10 kHz with an exposed time of 5  $\mu$ s. The PIV and OH\* signals were not measured simultaneously. Figure 2 presents the optical setup for PIV and OH\* measurements. For each case, 100 PIV images in 10 ms and 5000 OH\* images in 500 ms were obtained. The PIV results were post-processed using the open-source software PIVlab.<sup>23</sup> The uncertainty of the PIV measurement was evaluated using an *a posteriori* indirect approach called the peak-to-peak ratio (PPR) method.<sup>24</sup> The PPR is the ratio of the first peak to the second peak in a cross-correlation plane. It provides an upper limit of 0.41 pixel and a lower limit of 0.10 pixel at a confidence level of 68.5%. The uncertainty propagation was also evaluated via the Taylor series method.<sup>25</sup>

Methane was used as the fuel to create partially premixed combustion in this burner. The partially premixed burner consists of a pilot fuel injector with an inner swirler and the main fuel injector with an outer swirler. The swirl number is about 0.8 for both swirlers. The pilot fuel was injected through 6 holes with a diameter of 0.8 mm, and the main fuel was injected through 12 holes with a diameter of 1 mm. Two different partially premixed flames are investigated in this paper, and the operating conditions are summarized in Table I. The fuel stratification ratio (FSR) in this paper is defined as the ratio of the inner fuel mass flow to the outer fuel mass flow, which is not the same as the stratification ratio based on the equivalent ratio.<sup>26</sup> For case S1, the total airflow rate was fixed at 160 g/s and the total methane flow rate was 1.191 g/s, which lead to FSR = 1:1. While keeping the thermal power of about 56 kW as the same as S1, the FSR and total airflow rate of case S2 were changed to 1:9 and 290 g/s, respectively.

### III. NUMERICAL SETUP

Numerical calculations were carried out with a finite volume solver, and the large-eddy simulation (LES)-filtered Navier–Stokes equations can be written as

$$\begin{aligned} \frac{\partial \bar{p}}{\partial t} + \frac{\partial}{\partial x_i} (\bar{\rho} \bar{u}_i) &= \bar{S}_{mass}, & (1) \\ \frac{\partial}{\partial t} (\bar{\rho} \bar{u}_i) + \frac{\partial}{\partial x_j} (\bar{\rho} \bar{u}_i \bar{u}_j) &= -\frac{\partial \bar{p}}{\partial x_i} + \bar{\rho} g_i + \frac{\partial}{\partial x_j} (\bar{\sigma}_{ij}) \\ &\quad - \frac{\partial}{\partial x_j} (\bar{\tau}_{sgs}) + \bar{S}_{momentum}, & (2) \end{aligned}$$

where  $\bar{\sigma}_{ij}$ ,  $\bar{\tau}_{sgs}$ ,  $g_i$ ,  $\bar{\rho}$ ,  $\bar{u}_i$ , and  $\bar{p}$  represent the viscous stresses, sub-grid stress tensor, gravity, density, velocity, and pressure of the gas mixture. Over-bars and tildes represent spatially filtered and density-weighted filtered quantities based on a filter width  $\Delta$ , respectively. The turbulence subgrid-scale model is the dynamic Smagorinsky–Lilly model.<sup>27</sup> The detailed chemical kinetic mechanism used is described with 37 species and 227 reactions, and it is based on GRI-Mech 3.0.<sup>28</sup> The OH\* mechanism is added to the chemical kinetic mechanism. The complete set of OH\* formation and quenching reactions and rate constants used in this study is included in Table II. Rate coefficients are expressed as  $k = AT^b \exp(-E/RT)$  in units of cm, mol, s, and cal, where  $T$  is the equilibrium temperature of the medium.

To reduce the computational effort for solving additional equations for the species OH\* during the simulation run, the Flamelet Generated Manifold (FGM) model is considered here. In the FGM model, the tables that contain the combustion variables, e.g., species concentrations, temperature, density, and thermodynamic properties, are achieved using the flamelet approach. An ensemble of steady laminar premixed flamelets parameterized by mixture fraction  $Z$  and reaction progress  $c$  is generated in a two-dimensional subspace.<sup>34–36</sup> These equations are

$$\rho \frac{\partial Y_i}{\partial t} + \frac{\partial Y_i}{\partial c} \dot{\omega}_c - \rho \chi \frac{\partial^2 Y_i}{\partial c^2} = \dot{\omega}_i, \quad (3)$$

$$\begin{aligned} \rho \frac{\partial T_i}{\partial t} + \frac{\partial T_i}{\partial c} \dot{\omega}_c - \rho \chi \frac{\partial^2 T_i}{\partial c^2} &= \frac{\rho \chi}{C_p} \left( \frac{\partial C_p}{\partial c} + \sum_i^N C_{p,i} \frac{\partial Y_i}{\partial c} \right) \frac{\partial T_i}{\partial c} \\ &\quad - \frac{1}{C_p} \sum_i^N h_i \dot{\omega}_i, & (4) \end{aligned}$$

where  $Y_i$  is the  $i$ th species mass fraction,  $T_i$  is the temperature,  $\rho$  is the fluid density,  $t$  is the time,  $\dot{\omega}_i$  is the mass reaction rate,  $h_i$  is the total enthalpy, and  $C_{p,i}$  is the specific heat at constant pressure. The scalar dissipation rate is modeled as a prescribed function by using the value at stoichiometric mixture fractions  $\chi^{sto}$  and  $Z_{sto}$ . In order to include the turbulence–chemistry interactions, the filtered non-adiabatic combustion variables are retrieved by integrating over the joint probability density function (PDF) of reaction-progress  $c$  and mixture fraction  $Z$  as follows:

$$\tilde{\phi} = \int_0^\infty \int_0^\infty \phi(Z, c, \bar{h}) P(Z, c) df dc, \quad (5)$$

where  $\tilde{\phi}$  denotes the species mass fraction or temperature from the flamelet files.  $\bar{h}$  is the mean enthalpy. The joint PDF  $P(Z, c)$  is specified as the product of two beta PDFs.

**TABLE II.** Chemiluminescence reaction mechanisms to model OH\* formation and quenching and corresponding rate parameters.

R-No.	Reaction	A (mol cm <sup>-3</sup> s <sup>-1</sup> )	b	Ea (cal/mol)	Reference
R1	H + O + M = OH* + M	1.50 × 10 <sup>13</sup>	0.00	5966	29
R2	CH + O <sub>2</sub> = OH* + CO	8.000 × 10 <sup>10</sup>	0.00	0	30
R3	OH* = OH + hν	1.45 × 10 <sup>6</sup>	0.00	0	31
R4	OH* + O <sub>2</sub> = OH + O <sub>2</sub>	2.10 × 10 <sup>12</sup>	0.5	-482	32
R5	OH* + H <sub>2</sub> O = OH + H <sub>2</sub> O	5.93 × 10 <sup>12</sup>	0.5	-861	32
R6	OH* + H <sub>2</sub> = OH + H <sub>2</sub>	2.95 × 10 <sup>12</sup>	0.5	-444	32
R7	OH* + N <sub>2</sub> = OH + N <sub>2</sub>	1.08 × 10 <sup>11</sup>	0.5	-1238	32
R8	OH* + OH = OH + OH	6.01 × 10 <sup>12</sup>	0.5	-764	32
R9	OH* + H = OH + H	1.31 × 10 <sup>12</sup>	0.5	-167	32
R10	OH* + CO = OH + CO	3.23 × 10 <sup>12</sup>	0.5	-787	32
R11	OH* + CO <sub>2</sub> = OH + CO <sub>2</sub>	2.75 × 10 <sup>12</sup>	0.5	-968	32
R12	OH* + CH <sub>4</sub> = OH + CH <sub>4</sub>	3.36 × 10 <sup>12</sup>	0.5	-635	32
R13	OH* + O = OH + O	1.50 × 10 <sup>12</sup>	0.5	0	33

During the solution processing, the manifold data are recalled solving the following conservation equations:

$$\frac{\partial \bar{\rho} \tilde{Z}}{\partial t} + \frac{\partial}{\partial x_j} (\bar{\rho} \tilde{u}_j \tilde{Z}) = \frac{\partial}{\partial x_j} \left( \bar{\rho} (\tilde{D} + D_t) \frac{\partial \tilde{Z}}{\partial x_j} \right) + \bar{S}_z, \quad (6)$$

$$\frac{\partial \bar{\rho} \tilde{Y}_c}{\partial t} + \frac{\partial}{\partial x_j} (\bar{\rho} \tilde{u}_j \tilde{Y}_c) = \frac{\partial}{\partial x_j} \left( \bar{\rho} (\tilde{D} + D_t) \frac{\partial \tilde{Y}_c}{\partial x_j} \right) + \bar{\omega}_c. \quad (7)$$

In Eq. (6),  $\bar{S}_z$  represents the source term due to spray evaporation, whereas  $\bar{\omega}_c$  is the source term of the progress variable that has been modeled in the present study using a finite rate formulation.  $Y_c$  is the unscaled progress variable and is defined as  $Y_c = Y_{CO} + Y_{CO_2}$  in the present study. The variance of the unscaled reaction progress variable is modeled with a transport equation.

For the grid independence,  $23 \times 10^6$  coarse and  $66 \times 10^6$  fine unstructured tetrahedral meshes were compared. The  $66 \times 10^6$  meshes presented in Fig. 3(a) have been chosen to produce the main unsteady features of the flow field. The time step is set as  $1 \times 10^{-7}$  s. The minimum grid dimension is 100 μm near the fuel injection holes. In the flame region, the refined grid varies from 200 to 500 μm. To reduce the computational cost, the inlet section is set as 150 mm in length along the  $x$ -direction and removes small geometry details.

The height of the combustion section is 200 mm, and a pressure outlet is used. The sidewall of the combustor is estimated with a K-thermocouple and set to a constant temperature of 1500 K. The typical results of LES are shown in Fig. 3(b). For velocity comparison, the mean and root mean square (rms) values of lines  $x_1$ ,  $x_2$ , and  $x_3$  at 5.28, 24.64, and 77.44 mm are selected.

## IV. RESULTS AND DISCUSSION

### A. Non-reacting flow structures

The results of averaged unreacted flows are shown in Figs. 4 and 5. Figure 4 presents the time-averaged PIV and LES results of case S1. The  $x$ -direction and  $y$ -direction velocity fields with streamlines are compared. Generally, the numerical results show the same flow structure compared to the experimental average data. In Fig. 4, two large inner recirculation zones (IRZs) are located between the inner shear layers (ISLs). The outer recirculation zone (ORZ) lies at the corner under the outer shear layer (OSL). These flow structures have been widely studied for their stabilization of flame.<sup>37</sup> For case S2, Fig. 5 demonstrates a similar flow structure as case S1. However, due to the increase in the airflow rate, the strength of the inner shear layer is also increased. The impinging of the swirl flow on the sidewall leads to a separation of the large IRZ from the small vortex region.

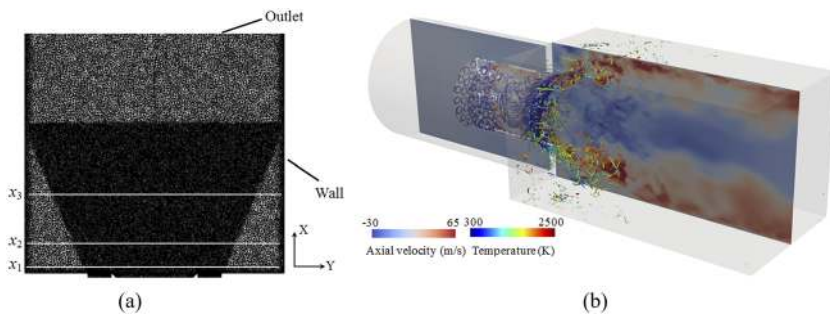


**FIG. 3.** (a) Cross section of the mesh grid and (b) diagram of the computation domain. The instantaneous axial velocity contour and temperature isosurface imposed on the Q criterion are shown.

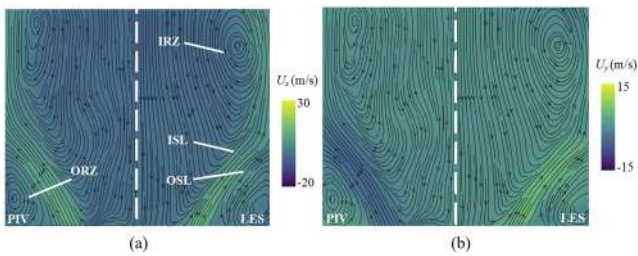


**FIG. 4.** Time-averaged PIV and LES results of the  $x$ -direction velocity field (a) and  $y$ -direction velocity field (b) with streamlines. The contours are the non-reacting flow of case S1.

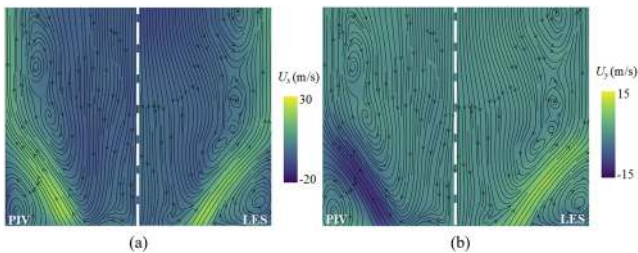


**FIG. 5.** Time-averaged PIV and LES results of the  $x$ -direction velocity field (a) and  $y$ -direction velocity field (b) with streamlines. The contours are the non-reacting flow of case S2.

Quantitative comparisons of  $x$  and  $y$  velocities between LES and PIV results are shown in Figs. 6 and 7. In general, the numerical values in Fig. 6 match well with the measured values. The main difference occurs at  $x = 24.64$  mm for the mean and rms of  $x$ -velocity. The experiment results show larger mean and rms values near  $y = 30$  mm, which lead to a wide IRZ near the central line of the combustion section. The same trend can be found in case S2 presented in Fig. 7. The slightly lower rms values for both cases indicate that the turbulence levels are underestimated by the simulations. A wider IRZ from the PIV measurement is also revealed through the velocity contour in Figs. 4 and 5. This may be due to a strong backflow near the sidewall. Overall, the cold flow for cases S1 and S2 shares a similar structure, which is natural since the main feature of the swirlers remains the same, and good agreement between measurements and simulations can be obtained.

## B. Reacting flow structure of two fuel stratification ratios

Figure 8 presents the typical flow and flame structure of stratified partially premixed swirl flame. Due to the existence of radical staged flame, two flame regions of the partially premixed flame are located downstream of the swirlers. The pilot flame in this paper is technically a non-premixed flame with a high equivalent ratio. Meanwhile, the main flame is technically premixed at an equivalent ratio of 0.7 through a relatively long mixed length in the outer swirl channel. Figure 9 shows the time-averaged PIV and LES results at a fuel stratification ratio of 1:1. The main flow structure of the

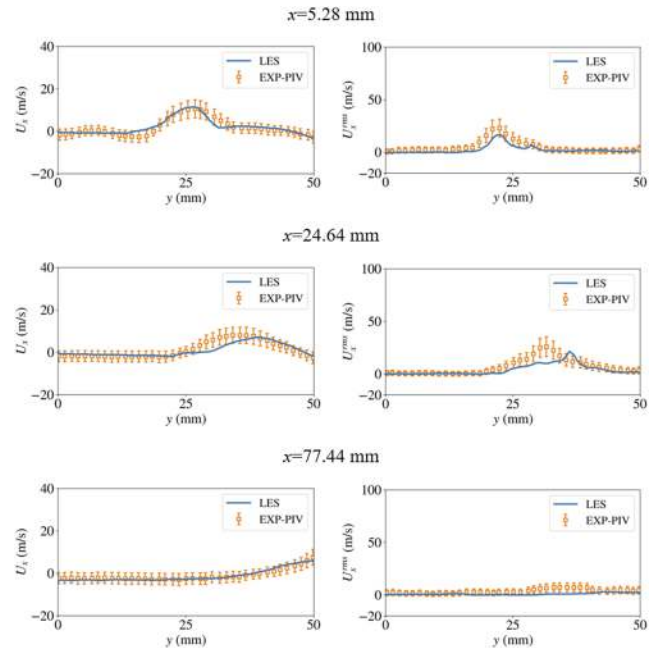


**FIG. 6.** The comparison of the mean and rms of  $x$ -direction velocity between PIV and LES results for case S1 at different  $x$  locations. The left column represents the mean  $x$ -velocity, while the right column represents the rms value of  $x$ -velocity.

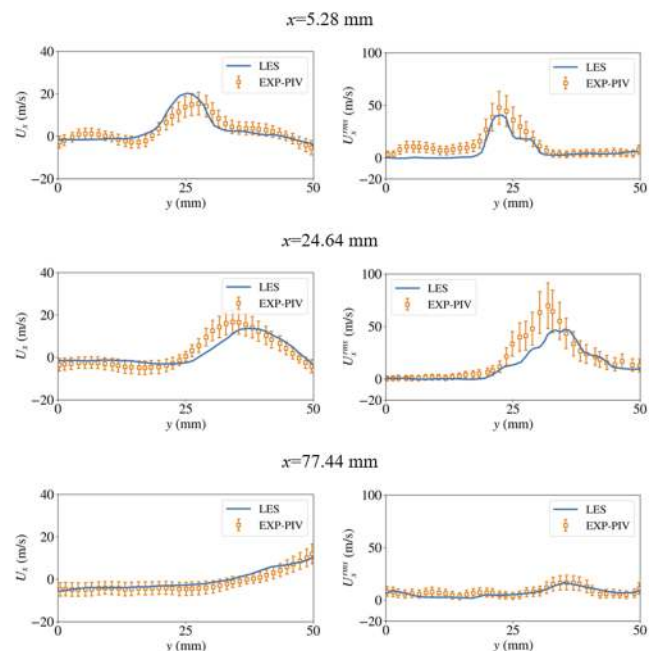


**FIG. 7.** The comparison of the mean and rms of  $x$ -direction velocity between PIV and LES results for case S2 at different  $x$  locations. The left column represents the mean  $x$ -velocity, while the right column represents the rms value of  $x$ -velocity.

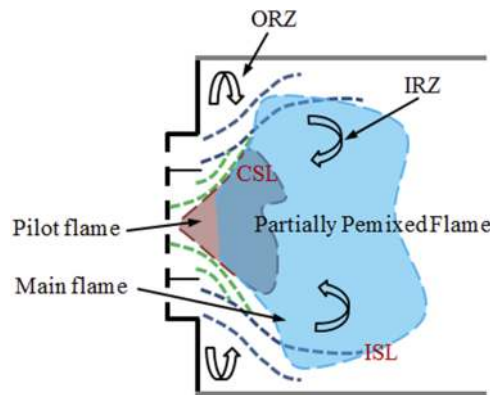


FIG. 8. Typical flow and flame structure of a stratified partially premixed swirl flame.

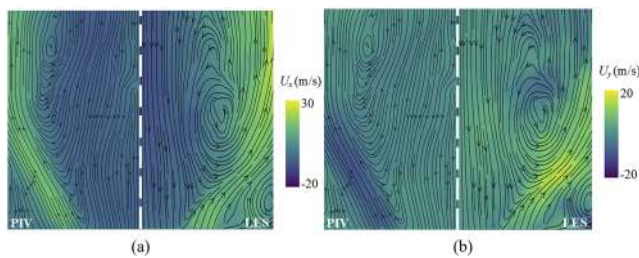


FIG. 9. Time-averaged PIV and LES results of the x-direction velocity field (a) and y-direction velocity field (b) with streamlines. The contours are the reacting flow of case S1 with a fuel stratification ratio of 1:1.

experiment and simulation is similar, while the location of the IRZ in experimental contours is higher than the numerical result. A much wider IRZ can also be observed in the LES results. The mean x-velocity comparison in Fig. 10 at  $x = 24.64$  mm shows the wider axial velocity distribution feature along the y-direction. From Figs. 4 and 9, we can find that the structure of non-reacting and reacting flows for case S1 stays the same shape. The existence of flame does not change the IRZ and ORZ significantly. The reason is that a high speed of pilot fuel near 270 m/s is injected, leading to a long penetration length, which emerges the pilot flame well with the main flame.

For the reacting flow of case S2, the existence of stratified flame creates a central recirculation zone (CRZ) and a central shear layer (CSL) in Fig. 11. Both the experimental and numerical results show the CRZ and CSL near the pilot flame. The CRZ and IRZ are clearly separated in case S2 compared to case S1 in Fig. 10. The pilot fuel injection speed is near 55 m/s, which is much lower than 270 m/s in case S1. Figure 12 shows the comparison of mean x-direction and y-direction velocities between PIV and LES results for case S2. The numerical values match well with the measurement data in general. However, a higher axial velocity can be obtained from PIV results, which is also revealed in Fig. 11. The upper bound of the effective strain rate defined in Ref. 38 is used to calculate the representative values of the strain rates. The assumption of circumferential

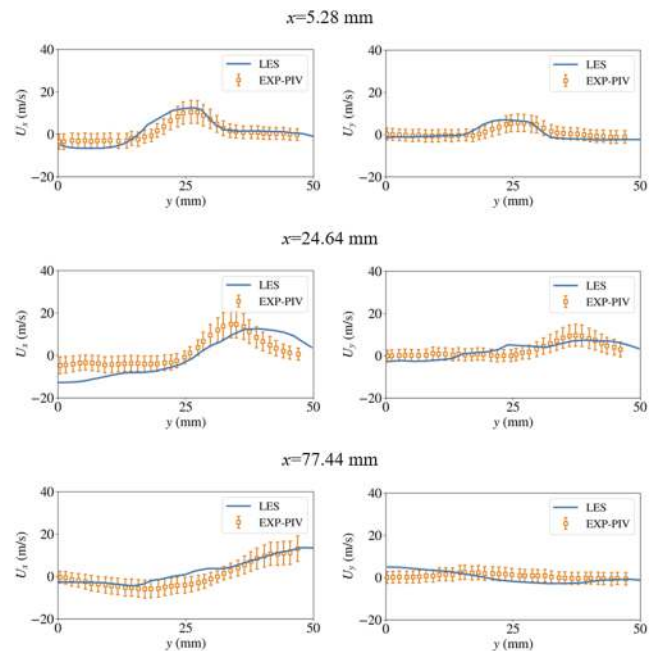


FIG. 10. The comparison of mean x-direction and y-direction velocities between PIV and LES results for case S1 at different x locations. The left column represents the mean x-velocity, and the right column represents the mean velocity along the y-axis.

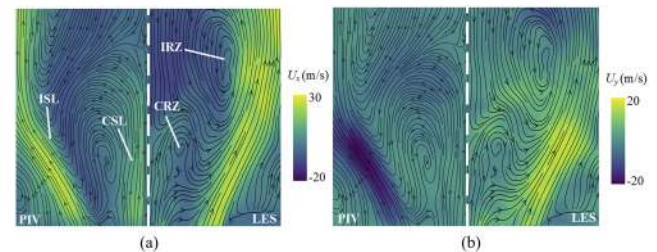
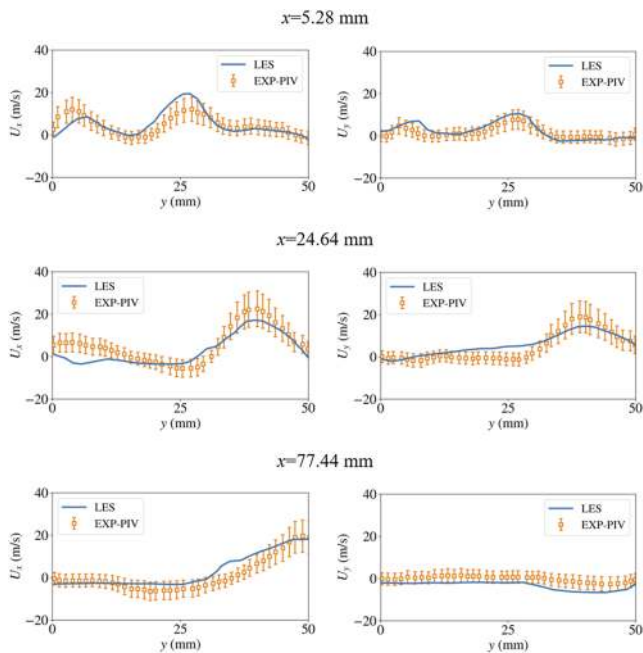


FIG. 11. Time-averaged PIV and LES results of the x-direction velocity field (a) and y-direction velocity field (b) with streamlines. The contours are the reacting flow of case S2 with a fuel stratification ratio of 1:9.

symmetry is made on averaged PIV data to map the 2D velocity vector to a cylindrical coordinate system,

$$\bar{\kappa}_{max} = \left| \frac{\partial U_x}{\partial x} \right| + \left| \frac{\partial U_r}{\partial x} + \frac{U_x}{r} + \frac{\partial U_x}{\partial r} \right| + \left| \frac{\partial U_r}{\partial r} + \frac{U_r}{r} \right|. \quad (8)$$

$\bar{\kappa}_{max}$  is then normalized by the inlet air velocity as a reference. Although it is a qualitative assessment framework, a more strong strain between the pilot and main flame can be observed in the FSR = 1:9 case. Moreover, the relative moderate strain rate exists in the pilot flame region between the CSL and ISL for case S2. This difference of strain rate effects on heat release and OH\* signals is discussed in Sec. IV C.



**FIG. 12.** The comparison of mean x-direction and y-direction velocities between PIV and LES results for case S2 at different x locations. The left column represents the mean x-velocity, and the right column represents the mean y-velocity.

### C. OH\* and heat release comparison

Figure 13 shows the OH\* filtered flame images at different FSRs. Both the averaged and Abel inverted images are presented. A V-type flame is observed in the case of S1, while the S2 flame exhibits a W type. These two distinguished flame shapes have a significant impact on the flow structure shown in Figs. 9 and 11. The S1 flame is stabilized due to the IRZ, and nearly non-CRZ occurs. However, the pilot and main flames in case S2 are separated. The pilot flame is stabilized near the CRZ, and the main flame lies near the ISL. To illustrate and compare the flame shape changes in different FSRs, the embedded OH\* mechanism simulation is performed in this paper. The contours of heat release, OH\* concentration, and OH\* concentration for cases S1 and S2 are shown in Fig. 14. It is obvious that

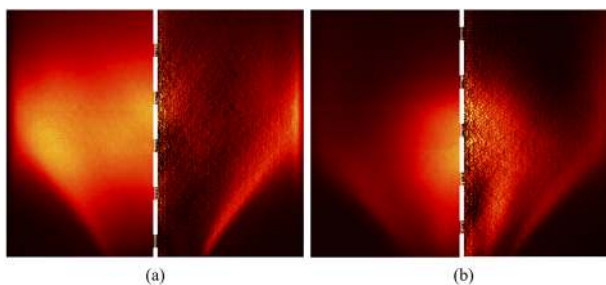


**FIG. 13.** (a) OH\* image of S1 flame and (b) OH\* image of S2 flame. The left parts of both S1 and S2 flame images are the time-averaged measurements. The right parts of both S1 and S2 flame images are presented after Abel inversion transform.

the OH\* contours differ from heat release in both cases. The distribution of heat release is much wider than the OH\* concentration. The results of both cases indicate that OH\* can only partially label the heat release zone, while the area of OH\* distribution covers the main feature of the heat release. The OH concentration is mainly located in the high temperature after-burn region, which has been verified by a lot of research.<sup>39,40</sup>

Figure 16 shows the time average results of the OH\* concentration obtained through the experiment and simulation. As mentioned before, the OH\* and heat release distributions are not identical. Figure 16(a) again reveals the same feature that the time-averaged OH\* contours can represent the most part of the heat release zones. A part of information related to heat release is still lost in the OH\* zones, especially in the ORZ of the flame. This phenomenon is further verified by the experimental result in Fig. 16(b). The heat release zone in the ORZ region is not clearly shown in the OH\* measurement. One reason is that the original weak signal strength of heat release in the ORZ of case S1 further vanishes in the OH\* signal. The same trend can be found in Fig. 17 of case S2. The major area of simulated OH\* overlaps the heat release zone. However, a weaker signal appears near the ORZ as the same as case S1. The OH\* signal in the pilot flame zone is not well reproduced by numerical simulation. The heights of numerical heat release and OH\* distribution are lower than the measured values. This may due to the low axial velocities resolved by LES in the pilot flame region (Figs. 11 and 12). In addition, comparing Figs. 15–17, it is found that the OH\* signals decrease in the strong strain rate region near shear layers for both cases. This implies that when analyzing the OH\* signals to correlating heat release distribution, the strain rate effects must be considered.

Overall, the time-averaged OH\* contour and heat release contour match well in most regions. However, for both cases, S1 and S2, the heat release locations in ORZ regions are not captured in OH\* simulation and measurement. This indicates that when using the OH\* chemiluminescence image as a spatial indicator of heat release, the wrong type of flame shape may be obtained near high strain rate regions. A weak M-type flame shape can be observed in both cases S1 and S2. In particular, when analyzing the strong unsteady motion, such as thermoacoustic instability, the recognition of the flame shape changing as a source of combustion instability should be carefully made by OH\* images.

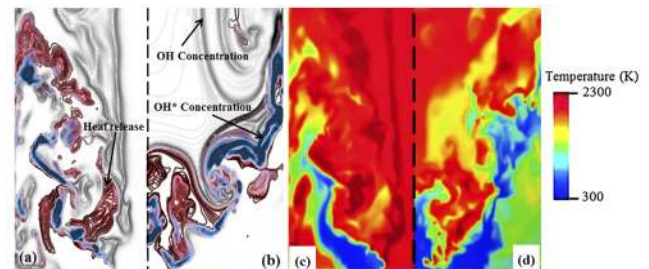


**FIG. 14.** Transient contours of heat release, OH\* concentration, and OH\* concentration for (a) case S1 and (b) case S2. The heat release is represented in red. The OH\* concentration is represented in blue and the OH concentration in gray. Transient contours of temperature for (c) case S1 and (d) case S2 are shown.



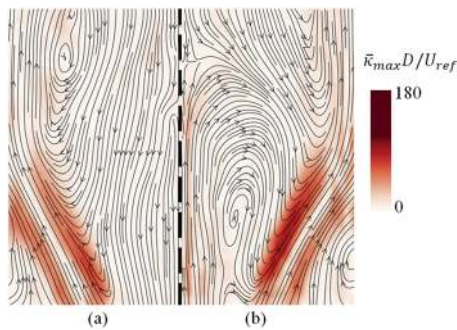


**FIG. 15.** Streamlines superimposed on contours of the normalized maximum effective strain rate: (a) FSR = 1:1 and (b) FSR = 1:9.

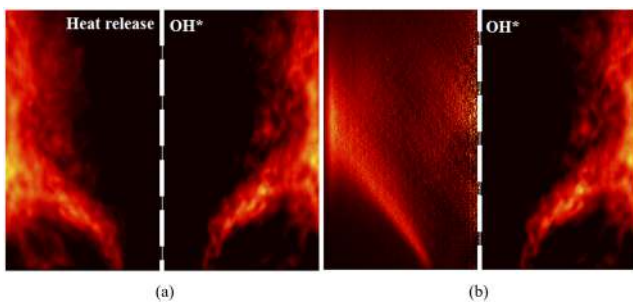


**FIG. 16.** Time average results of case S1: (a) numerical heat release and OH\* contours and (b) measured OH\* distribution (left) and simulated OH\* (right).

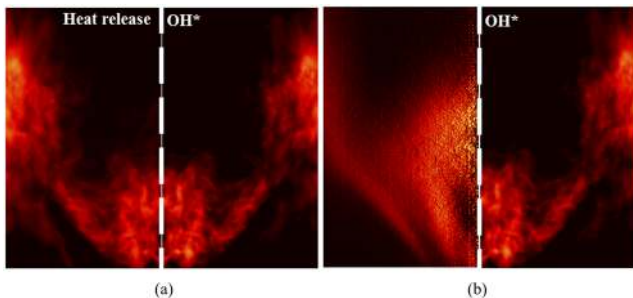


**FIG. 17.** Time average results of case S2: (a) numerical heat release and OH\* contours and (b) measured OH\* distribution (left) and simulated OH\* (right).

## V. CONCLUSION

In this paper, the flow structure and heat release rate of stratified swirl flames at two distinguished fuel stratification ratios are studied. 10 kHz PIV images and OH\* filtered images are recorded during the experiment. For non-reacting flow, the two airflow rate cases show the same flow pattern with the inner recirculation zone and outer recirculation zone. A large inner recirculation zone is found in 1:1 FSR reacting case S1, while both the central recirculation zone and inner recirculation zone appear in 1:9 FSR reacting case S2. This difference leads to a V-type flame for case S1 and a W-type flame for case S2.

A large-eddy simulation with detailed OH\* chemiluminescence reaction mechanisms is performed. In general, the velocity results of LES have good agreement with the measurement. The simulated heat release region has a wider area than simulated OH\* signals in the instantaneous contour. Nevertheless, the time-averaged results show a similar distribution between these two values. Only near the outer recirculation zone, the reduction of OH\* signals is shown for different FSRs. This indicates that the strain rate in different regions of stratified swirl flame may have a significant impact on OH\* signal distribution. As stated in Ref. 19, the turbulence reduces the chemiluminescence intensity more strongly than the heat release rate. Thus, the local heat release rate of a turbulent flame cannot be determined reliably from the uncorrelated OH\* chemiluminescence measurement. For case S2, the strain rates near the CSL and ISL are relatively high. The OH\* signal decreases significantly in those regions compared to heat release distribution.

It is also noticed that the wrong flame shapes may be deduced from the Abel inverted OH\* image since the signals are weak in the outer recirculation zone. It is also validated by the LES results. This phenomenon should be investigated in further research by using simultaneous measurements, such as OH/CH<sub>2</sub>O planar laser-induced fluorescence (PLIF). For combustors with limited optical windows, OH\* signals can still give a reference of heat release distribution in time-averaged or phase averaged senses where the instantaneous strain rate effects are not significant. Moreover, the detailed chemistry radiation model for OH\* simulation offers an alternate method to facilitate and validate the numerical analysis since it can be compared directly to measured data.

## ACKNOWLEDGMENTS

This work is supported by the National Natural Science Foundation of China (Grant Nos. 51776191 and 52076136). This work is also supported by the National Science and Technology Major Project (Grant No. J2019-III-0002-0045).

## DATA AVAILABILITY

The data that support the findings of this study are available on request from the corresponding author. The data are not publicly available due to privacy restrictions.

## REFERENCES

- J. E. Temme, P. M. Allison, and J. F. Driscoll, "Combustion instability of a lean premixed prevaporized gas turbine combustor studied using phase-averaged PIV," *Combust. Flame* **161**, 958–970 (2014).
- N. Syred and J. M. Beér, "Combustion in swirling flows: A review," *Combust. Flame* **23**, 143–201 (1974).
- X. Han, D. Laera, A. S. Morgans, C. J. Sung, X. Hui, and Y. Z. Lin, "Flame macrostructures and thermoacoustic instabilities in stratified swirling flames," *Proc. Combust. Inst.* **37**, 5377–5384 (2019).
- M. P. Auer, C. Gebauer, K. G. Mösl, C. Hirsch, and T. Sattelmayer, "Feedback of combustion instabilities on the injection of gaseous fuel," *J. Eng. Gas Turbines Power* **127**, 748–754 (2005).
- M. Konle and T. Sattelmayer, "Time scale model for the prediction of the onset of flame flashback driven by combustion induced vortex breakdown," *J. Eng. Gas Turbines Power* **132**, 041503 (2010).
- K. T. Kim, J. G. Lee, B. D. Quay, and D. A. Santavicca, "Spatially distributed flame transfer functions for predicting combustion dynamics in lean premixed gas turbine combustors," *Combust. Flame* **157**, 1718–1730 (2010).

- <sup>7</sup>S. Tachibana, K. Saito, T. Yamamoto, M. Makida, T. Kitano, and R. Kurose, "Experimental and numerical investigation of thermo-acoustic instability in a liquid-fuel aero-engine combustor at elevated pressure: Validity of large-eddy simulation of spray combustion," *Combust. Flame* **162**, 2621–2637 (2015).
- <sup>8</sup>G. Vignat, D. Durox, K. Prieur, and S. Candel, "An experimental study into the effect of injector pressure loss on self-sustained combustion instabilities in a swirled spray burner," *Proc. Combust. Inst.* **37**, 5205–5213 (2018).
- <sup>9</sup>Y. Hardalupas and M. Orain, "Local measurements of the time-dependent heat release rate and equivalence ratio using chemiluminescent emission from a flame," *Combust. Flame* **139**, 188–207 (2004).
- <sup>10</sup>G. P. Smith, J. Luque, C. Park, J. B. Jeffries, and D. R. Crosley, "Low pressure flame determinations of rate constants for OH\* and CH\* chemiluminescence," *Combust. Flame* **131**, 59–69 (2002).
- <sup>11</sup>Y. Hardalupas, C. S. Panoutsos, and A. M. K. P. Taylor, "Spatial resolution of a chemiluminescence sensor for local heat-release rate and equivalence ratio measurements in a model gas turbine combustor," *Exp. Fluids* **49**, 883–909 (2010).
- <sup>12</sup>T. Kathrotia, U. Riedel, A. Seipel, K. Moshhammer, and A. Brockhinke, "Experimental and numerical study of chemiluminescent species in low-pressure flames," *Appl. Phys. B* **107**, 571–584 (2012).
- <sup>13</sup>C. D. Slabaugh, A. C. Pratt, and R. P. Lucht, "Simultaneous 5 kHz OH-PLIF/PIV for the study of turbulent combustion at engine conditions," *Appl. Phys. B* **118**, 109–130 (2015).
- <sup>14</sup>P. H. Paul and H. N. Najm, "Planar laser-induced fluorescence imaging of flame heat release rate," *Proc. Combust. Inst.* **27**, 43–50 (1998).
- <sup>15</sup>C. A. Fugger, S. Roy, A. W. Caswell, B. A. Rankin, and J. R. Gord, "Structure and dynamics of CH<sub>2</sub>O, OH, and the velocity field of a confined bluff-body premixed flame, using simultaneous PLIF and PIV at 10 kHz," *Proc. Combust. Inst.* **37**, 1461–1469 (2019).
- <sup>16</sup>C. D. Carter, G. B. King, and N. M. Laurendeau, "Saturated fluorescence measurements of the hydroxyl radical in laminar high-pressure C<sub>2</sub>H<sub>6</sub>/O<sub>2</sub>/N<sub>2</sub> flames," *Appl. Opt.* **31**, 1511–1522 (1992).
- <sup>17</sup>T. Fiala and T. Sattelmayer, "Assessment of existing and new modeling strategies for the simulation of OH\* radiation in high-temperature flames," *CEAS Space J.* **8**, 47–58 (2016).
- <sup>18</sup>M. Lauer and T. Sattelmayer, "On the adequacy of chemiluminescence as a measure for heat release in turbulent flames with mixture gradients," *J. Eng. Gas Turbines Power* **132**, 061502 (2010).
- <sup>19</sup>M. Lauer, M. Zellhuber, T. Sattelmayer, and C. J. Aul, "Determination of the heat release distribution in turbulent flames by a model based correction of OH\* chemiluminescence," *J. Eng. Gas Turbines Power* **133**, 121501 (2011).
- <sup>20</sup>M. J. Bedard, T. L. Fuller, S. Sardeshmukh, and W. E. Anderson, "Chemiluminescence as a diagnostic in studying combustion instability in a practical combustor," *Combust. Flame* **213**, 211–225 (2020).
- <sup>21</sup>L. He, Q. Guo, Y. Gong, F. Wang, and G. Yu, "Investigation of OH\* chemiluminescence and heat release in laminar methane-oxygen co-flow diffusion flames," *Combust. Flame* **201**, 12–22 (2019).
- <sup>22</sup>Y. Liu, J. Tan, H. Wang, and L. Lv, "Characterization of heat release rate by OH\* and CH\* chemiluminescence," *Acta Astronaut.* **154**, 44–51 (2019).
- <sup>23</sup>W. Thielicke and E. J. Stamhuis, "PIVlab—Towards user-friendly, affordable and accurate digital particle image velocimetry in MATLAB," *J. Open Res. Software* **2**, e30 (2014).
- <sup>24</sup>Z. Xue, J. J. Charonko, and P. P. Vlachos, "Particle image velocimetry correlation signal-to-noise ratio metrics and measurement uncertainty quantification," *Meas. Sci. Technol.* **25**, 115301 (2014).
- <sup>25</sup>B. M. Wilson and B. L. Smith, "Taylor-series and Monte-Carlo-method uncertainty estimation of the width of a probability distribution based on varying bias and random error," *Meas. Sci. Technol.* **24**, 035301 (2013).
- <sup>26</sup>K. T. Kim and S. Hochgreb, "Effects of nonuniform reactant stoichiometry on thermoacoustic instability in a lean-premixed gas turbine combustor," *Combust. Sci. Technol.* **184**, 608–628 (2012).
- <sup>27</sup>D. K. Lilly, "A proposed modification of the Germano subgrid-scale closure model," *Phys. Fluids* **4**, 633–635 (1992).
- <sup>28</sup>G. P. Smith, D. M. Golden, M. Frenklach, N. W. Moriarty, B. Eiteneer, M. Goldenberg, C. T. Bowman, R. K. Hanson, S. Song, W. C. Gardiner, Jr., V. V. Lissianski, and Z. Qin, GRI-Mech 3.0, [http://www.me.berkeley.edu/gri\\_mech/](http://www.me.berkeley.edu/gri_mech/), 2017.
- <sup>29</sup>T. Kathrotia, M. Fikri, M. Bozkurt, M. Hartmann, U. Riedel, and C. Schulz, "Study of the H + O + M reaction forming OH\*: Kinetics of OH\* chemiluminescence in hydrogen combustion systems," *Combust. Flame* **157**, 1261–1273 (2010).
- <sup>30</sup>M. Bozkurt, M. Fikri, and C. Schulz, "Investigation of the kinetics of OH\* and CH\* chemiluminescence in hydrocarbon oxidation behind reflected shock waves," *Appl. Phys. B* **107**, 515–527 (2012).
- <sup>31</sup>W. L. Dimpfl and J. L. Kinsey, "Radiative lifetimes of OH (A<sup>2</sup>Σ) and Einstein coefficients for the A-X system of OH and OD," *J. Quant. Spectrosc. Radiat. Transfer* **21**, 233–241 (1979).
- <sup>32</sup>M. Tamura, P. A. Berg, J. E. Harrington, J. Luque, J. B. Jeffries, G. P. Smith, and D. R. Crosley, "Collisional quenching of CH(A), OH(A), and NO(A) in low pressure hydrocarbon flames," *Combust. Flame* **114**, 502–514 (1998).
- <sup>33</sup>V. N. Nori and J. M. Seitzman, "CH\* chemiluminescence modeling for combustion diagnostics," *Proc. Combust. Inst.* **32**, 895–903 (2009).
- <sup>34</sup>M. Ihme and H. Pitsch, "Modeling of radiation and nitric oxide formation in turbulent nonpremixed flames using a flamelet/progress variable formulation," *Phys. Fluids* **20**, 055110 (2008).
- <sup>35</sup>P.-D. Nguyen, L. Vervisch, V. Subramanian, and P. Domingo, "Multi-dimensional flamelet-generated manifolds for partially premixed combustion," *Combust. Flame* **157**, 43–61 (2010).
- <sup>36</sup>G. Lodier, L. Vervisch, V. Moureau, and P. Domingo, "Composition-space premixed flamelet solution with differential diffusion for in situ flamelet-generated manifolds," *Combust. Flame* **158**, 2009–2016 (2011).
- <sup>37</sup>M. S. Sweeney, S. Hochgreb, M. J. Dunn, and R. S. Barlow, "The structure of turbulent stratified and premixed methane/air flames II: Swirling flows," *Combust. Flame* **159**, 2912–2929 (2012).
- <sup>38</sup>S. J. Shanbhogue, Y. S. Sanusi, S. Taamallah, M. A. Habib, E. M. A. Mokheimer, and A. F. Ghoniem, "Flame macrostructures, combustion instability and extinction strain scaling in swirl-stabilized premixed CH<sub>4</sub>/H<sub>2</sub> combustion," *Combust. Flame* **163**, 494–507 (2016).
- <sup>39</sup>G. Singh, M. Juddoo, A. Kourmatzis, M. J. Dunn, and A. R. Masri, "Heat release zones in turbulent, moderately dense spray flames of ethanol and biodiesel," *Combust. Flame* **220**, 298–311 (2020).
- <sup>40</sup>S. Mohammadnejad, P. Vena, S. Yun, and S. Kheirkhah, "Internal structure of hydrogen-enriched methane-air turbulent premixed flames: Flamelet and non-flamelet behavior," *Combust. Flame* **208**, 139–157 (2019).